Detection of biological macromolecules on a biochip dedicated to UV specific absorption

Kristelle Robin, Jean-Luc Reverchon, Laurent Mugherli, Michel Fromant, Pierre Plateau, Henri Benisty

Detection of biological macromolecules on a biochip dedicated to UV specific absorption

Kristelle Robin [a,*], Jean-Luc Reverchon [a], Laurent Mugherli [b], Michel Fromant [b], Pierre Plateau [b], Henri Benisty [c]

[a] *Thales Research and Technology, RD 128, 91767 Palaiseau Cedex, France*
[b] *Laboratoire de Biochimie, Ecole Polytechnique, CNRS, 91128 Palaiseau Cedex, France*
[c] *Laboratoire Charles Fabry de l'Institut d'Optique, Campus Polytechnique, RD 128, 91127 Palaiseau Cedex, France*

This work describes an ultraviolet biosensing technique based on specific molecular absorption detected with a previously developed spectrally selective aluminum gallium nitride (AlGaN) based detector. Light absorption signal of DNA and proteins, respectively at 260 nm and 280 nm, is used to image biochips. To allow detection of protein or DNA monolayers at the surface of a biochip, we develop contrast-enhancing multilayer substrates. We analyze them through models and experiments and validate the possibility of measuring absorptions of the order of 10^{-3}. These multilayer structures display a high reflectivity, and maximize the interaction of the electric field with the biological element at the chip surface. Optimiza-tion of the experimental absorption, which includes effects such as roughness of the biochip, spectral and angular resolution of the optics, illumination, etc., is carried out with an inorganic ultraviolet absorber (titanium dioxide) deposit. We obtained an induced absorption contrast enhanced by a factor of 4.0, confer-ring enough sensitivity to detect monolayers of DNA or proteins. Experimental results on an *Escherichia coli* histidine-tagged methionyl-tRNA synthetase protein before and after complexation with an anti-polyHis specific antibody validate our biosensing technique. This label-free optical method may be helpful in controlling biochip coatings, and subsequent biological coupling at the surface of a biochip.

1. Introduction

1.1. Label-free optical biosensors

Biosensors detect and quantify target compounds. They involve a biological molecule intimately connected to a transducer, which can be of diverse nature. For optical detection, fluorescent labels are often used to report binding events. However, labeling is expensive and time consuming. Moreover, hydrophobic fluorophores can cause false binding and lead to false positives. Thus, optical label-free biosensors are presently of foremost interest.

The most widespread label-free optical sensors exploit surface plasmon resonance (Smith and Corn, 2003). A drawback of this method is the metallic surface, which often induces non-specific interactions.

An alternative method is ultraviolet (UV) imaging. An advantage of UV imaging is the possible use of dielectric surface, to limit non-specific interactions. Absorption of DNA and proteins at 260 nm and 280 nm is widely used to measure their concentration in solution. This absorption may also reveal biological compounds present at the surface of a substrate or a chip. To provide a good sensitivity and minimize UV illumination, the intrinsically weak optical contrast of surface absorption signal has to be optimized. This paper shows the feasibility of this approach, including optical, technological and biochemical aspects.

1.2. Absorption of DNA and proteins in UV

We start with a quantification of the useful DNA and protein absorption. To get rid of unwieldy size effects in molar absorption, we use mass absorption.

1.2.1. DNA absorption at 260 nm

Fig. 1(a) gives the absorbance spectra of the four nucleotides composing DNA (water, pH 7, Du et al., 1998). For an equimolar nucleotidic composition, absorbance peaks at a wavelength $\lambda = 260$ nm. For single-stranded DNA (ssDNA) specific absorption is $\varepsilon_{260\,\mathrm{nm}} = 0.027\ \mathrm{cm}^2/\mu\mathrm{g}$ (300 mM potassium phosphate buffer, pH

* Corresponding author. Tel.: +33 1 69 41 58 01; fax: +33 1 69 41 57 38.
E-mail address: kristelle.robin@thalesgroup.com (K. Robin).

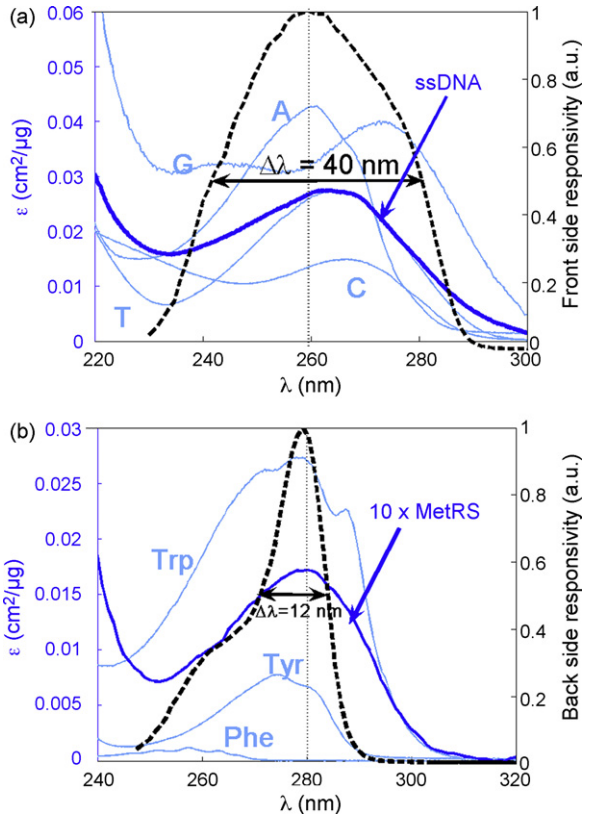

Fig. 1. (a) (solid line) Nucleotide and single stranded DNA absorption spectra, and (dashed line) responsivity spectra of the spectrally selective AlGaN detector for front side illumination. (b) (solid line) Aromatic amino acid and MetRS absorption spectra, and (dashed line) responsivity of the detector for back side illumination.

7, Fasman, 1975). The absorbance A_λ is given by the Beer-Lambert law:

$$A_\lambda = -\log\left(\frac{I_\lambda}{I_{\lambda_0}}\right) = \varepsilon_\lambda\, l\, c \qquad (1)$$

with c the mass concentration in $\mu g/cm^3$, l the path length in cm, I_{λ_0} and I_λ the intensities without and with absorber, and ε_λ the mass extinction coefficient at the wavelength λ in $cm^2/\mu g$.

Considering $l = 1$ cm, we can express A_λ as a surface absorption related to the surface density lc. Typical densities of DNA probes lie from 2×10^{12} to 1.2×10^{13} molecules/cm^2 (Peterson et al., 2001). The absorbance values at 260 nm are given in Table 1. The target absorption ranges from 1.9×10^{-3} (70 bases, density 2×10^{12} molecules/cm^2) to 7.9×10^{-2} (500 bases, density 1.2×10^{13} molecules/cm^2).

1.2.2. Protein absorption at 280 nm

For a similar mass, protein absorption at 280 nm is roughly one order of magnitude smaller than that of DNA at 260 nm (depending on the amino acid sequence (Gill and von Hippel, 1989; Pace et al., 1995) and on the nucleotide sequence (Fasman, 1975)). Proteins absorb UV light in proportion to their aromatic amino acids content. This absorption is roughly centered at 280 nm. As an example, we consider here a histidine-tagged methionyl-tRNA synthetase (MetRS). The MetRS protein, whose $\varepsilon_{280\,nm}$ is 1.72×10^{-3} cm$^2/\mu g$ (Cassio and Waller, 1971), is used in the experiments of Section 3. Fig. 1(b) gives the experimental absorption spectrum of MetRS (20 mM potassium phosphate buffer, pH 8.5) and of the aromatic amino acids (measured in water, pH 7 for phenylalanine, and in 100 mM phosphate buffer, pH 7 for tyrosine and tryptophan (Du et al., 1998)).

In solution, the MetRS protein occupies a volume of 5 nm × 5 nm × 10 nm (Mechulam et al., 1999). Thus, the minimum surface per one MetRS molecule is 5 nm × 5 nm, and consequently, the maximum density reached for a monolayer coverage, is 4×10^{12} molecules/cm^2, or 0.4 $\mu g/cm^2$. This yields an absorption in transmission of only $A_{280\,nm} = 0.73 \times 10^{-3}$, too small for standard measurement techniques and thus calling for enhancement methods. As an example, absorbance values at 280 nm of MetRS and anti-polyHis antibody (antiHis-Ab), whose $\varepsilon_{280\,nm}$ is 1.47×10^{-3} cm$^2/\mu g$ (see Section 2.3.3) are given in Table 1.

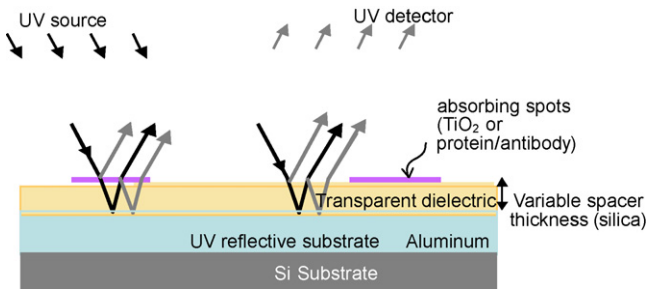

Fig. 2. Biochip and set-up.

2. Materials and methods

We present the UV imaging setup, and evaluate its noise and instrumental resolution limitations. Design, fabrication and assessment of contrast enhancing biochips are then described, followed by biological assay preparation.

2.1. Imaging set-up

2.1.1. Reflection set-up

Experiments are based on a reflection set-up composed of a lamp with Köhler illumination, the sample and a camera. Köhler illumination avoids glare from the source, with a controlled illuminating flux (Murphy, 2001). The camera detector is a linear array, perpendicular to the set-up plane. Placing the sample on a translation stage, successive lines are acquired to reconstruct a full chip image. Fig. 2 gives a scheme of the set-up and the biochip.

2.1.2. Instrumental resolution

2.1.2.1. Objective: angular resolution. The Olympus objective numerical aperture is NA = 0.1, corresponding to an angular

Table 1
Absorbance values of (a) single-stranded DNA (70 bases and 500 bases) at 260 nm and (b) MetRS and antiHis-Ab at 280 nm

Density (molecules/cm^2)	(a) DNA absorption, $A_{260\,nm} \times 10^3$		(b) Protein absorption, $A_{280\,nm} \times 10^3$	
	70 bases, 23 kDa	500 bases, 163 kDa	MetRS, 64 kDa	antiHis-Ab, 150 kDa
2×10^{12}	1.9	13.7	0.37	0.73
4×10^{12}	3.8	27.2	0.73	1.47
1.2×10^{13}	11.5	79.5	2.2	4.40

aperture $2\alpha = 11.4^\circ$, α being the half-cone angle. At $\lambda = 280$ nm, according to the Rayleigh criterion, this NA translates into an object plane resolution of 1.4 μm. Given the detector pitch of 26 μm and a $\gamma = 3.8$ magnification providing a 26/3.8–7 μm resolution in the object plane, diffraction is by far not a limiting factor. Resolution would be increased by using a smaller pixel pitch or an objective with larger magnification.

2.1.2.2. Camera: spectral resolution. Our AlGaN detector is a linear array of 300 pixels, with CCD readout circuits (Maezzo et al., 2006). Fig. 1(a) and (b) gives the spectral responsivity of the detector for a bias of 4 V, superposed to the biological absorption spectra. A detailed description of the internal structure of the pixel and of the spectral responses is reported in Maezzo et al. (2006). For front side illumination, the spectral responsivity is centered at 260 nm, and applies well to DNA assay (Reverchon et al., 2006). For back side illumination, the responsivity centered at 280 nm and applies better to protein assay. The spectral selectivity (40 nm for front side, 12 nm for back side) enables to measure the contribution around the absorption maximum, and to have a sensitive measure.

2.1.3. Noise effects on detection limit

As shown in Section 1.2, a monolayer of proteins induces a single-pass absorption of 10^{-3}. A limitation to detect such a low absorption is photon and electrical noise arising from the UV source and from the detector.

Concerning the illumination, the Xenon lamp displays a flash-to-flash output stability of about 3%. For a $\tau = 100$ ms integration time, at 200 Hz flash frequency, it causes a relative noise of $3\%/\sqrt{20} = 0.7\%$, reduced to 0.2% when further averaging over 10 frames. Limitation in sensitivity arises from different contributions in the noise of the photodiode array (Maezzo et al., 2006). The 7 mV electrical noise is not due to the detector itself, but to the readout and polarization circuitry. With an output saturation voltage of 7 V but an actual output of 5 V for convenience, the dynamic range ratio is about 700 (5 V/7 mV). Hence, a dynamic range ratio above 10^3 is possible by averaging a few successive images.

2.1.4. Non-uniformity correction

Non-uniformities among the responsivity of pixels are a severe problem in arrays of photodiodes. They result in a fixed-pattern "noise", which needs to be corrected. Firstly, in the dark, a readout offset correction is realized separately on the two CCD circuits. Subsequently, a gain correction is carried out. To normalize the array, or "flatten it", each pixel signal is divided by its corresponding gain. A gain calibration frame is obtained by Köhler illumination of a uniform sample. All subsequent frames are divided by this calibration frame, reducing the 5% pixel-to-pixel gain variation to an acceptable 0.6% variation.

2.1.5. Image conversion limitation

A required specification to detect minute contrasts (10^{-3}) is bit depth. Sensors used here have 12-bit (4096) analog-to-digital converters, so digitization noise is usually not an issue at the sensor level. Each line of the image is the average over at least 10 frames with a dynamical range growing from 12 to 16 bits (65536). Thus, the result is not limited by conversion noise.

2.2. Design and properties of specific slides

We describe here the design of the contrast-enhancing substrate which makes our biochip viable for detection of biological ultraviolet absorbers. The design uses the knowledge of the electromagnetic field structure to get stronger electromagnetic interactions at the chip surface.

2.2.1. Basic design

The biochip is a UV reflective multilayer structure. It consists in a UV reflective metal, covered with transparent dielectric for both contrast enhancement and biocompatibility. The dielectric used here is silica, with index $n_d = 1.495$. The thickness e of the dielectric layer has to maximize the local electric field at the surface to enhance the absorption of the biological entity. It is well known that standing waves at normal incidence have antinodes spaced by a half wavelength optical thickness (the optical thickness is then just $n_d \times e$). Above a perfect metallic mirror, the first antinode lies at a quarter wavelength optical thickness. A basic normal incidence design thus consists in coating such an optical thickness above the metal, so that the biological entity is located at the antinode. For a perfect standing wave (doubled amplitude $1 + \sqrt{R} \cong 2$ at antinode, due to constructive interference (Seraphin and Bottka, 1965; Benisty et al., 1998)), absorption contrast is enhanced by a factor 4.

In practice, experiments differ from this model. First, at non-normal incidence, the optical path comprises a factor $\cos\theta'$ where θ' is the refracted angle in the dielectric, $\theta' = \arcsin(\sin\theta/n_d)$. For our case $\theta = 45^\circ$, $\theta' = 28^\circ$. Second, the metal has a penetration depth $\delta_{Al}(\theta, n_d)$, defining an effective plane inside the metal where the wave is apparently reflected (Bass et al., 2000). The more general quarter wave condition thus reads:

$$n_d\, e \cos\theta' + \delta_{Al}(\theta, n_d) = \frac{\lambda}{4} \tag{2}$$

The wave exponentially vanishes in the metal. The penetration depth δ_{Al} is quantitatively defined as the depth at which the squared electric field inside the metal falls to $1/e$ of its surface value (Bass et al., 2000). At normal incidence, its expression is $\delta_{Al} = \lambda/(2\pi k)$, where k denotes the imaginary part of the refractive index $\tilde{n}_{Al} = n + ik$. At $\lambda = 280$ nm, $\tilde{n}_{Al} = 0.23 + 3.36i$, corresponding to $\delta_{Al} = 13.3$ nm. In reality, due to the oxidation and roughness of the aluminum film (Smith et al., 1985), the optical penetration in the aluminum is deeper. This is modeled by an extra thin layer at the aluminum surface, defined in the Bruggeman method (Bruggeman, 1935; Stroud, 1998). This layer is composed of alumina and aluminum. The main trend induced by alumina inclusions is to increase the electric field penetration in the structure, and to diminish reflectivity.

2.2.2. Optical properties determination

The experimental optical properties such as reflectance, transmittance, absorbance are assessed by modeling the multilayer sample. Their optical response functions $F(\theta,\lambda)$ are calculated using IMD software (Windt, 1998). However, data are acquired in practice with limited angular and/or spectral resolution, possibly diminishing the contrast much as in two-wave interferometers, Michelson type or others. The resolution-limited values are taken into account by convolving the optical functions with a Gaussian of width $\Delta\theta$ for the angular resolution of the camera, and $\Delta\lambda$ for the sensitivity of the linear array.

The spectral resolution of our detector is $\Delta\lambda = 40$ nm for front side illumination centered at $\lambda = 260$ nm ($\Delta\lambda/\lambda = 15\%$), and $\Delta\lambda = 12$ nm for back-side illumination centered at $\lambda = 280$ nm ($\Delta\lambda/\lambda = 4.3\%$). The spectral responsivity mainly depends on the AlGaN multilayer composition. In transparent dielectric of index n_d, the interference order m is given by $m = 2n_d\, e\cos(\theta')/\lambda$ For a nominal interference order, the absolute change in interference order is $0.15m$ for backside, and $0.043m$ for front side.

A full excursion of $\Delta m = 0.25$ is needed to diminish the antinode contrast by 10%, which happens for roughly $m = 2$ for front side, and

$m = 6$ for back side. Since our basic design works at $m = 0.5$, we have a large margin, and virtually retain 100% of the antinode effect.

A similar approach holds for the angular resolution. For our set-up, the angular variation being $\Delta\theta = 11.4^\circ$ around 45° in air, $\cos(\theta')$ spans the interval 0.63–0.77, causing a change in interference order of $0.2m$. Consequently, the decrease in antinode contrast is less than 10% for our quarter wave design.

2.3. Chip fabrication and preparation

Calibration "bio"chips are first fabricated with a known inorganic absorber (titanium dioxide). Similar biochips are then functionalized, coated with MetRS and further complexed with an antiHis-Ab.

2.3.1. Slide fabrication and characterization

Aluminum is first deposited by thermal vacuum evaporation on a silicon wafer. Silica is next deposited by plasma enhanced chemical vapor deposition (PECVD) at 340 °C. To obtain variable silica thicknesses on the same sample, successive masked etching are realized by reactive ion etching (RIE). The mask provides stripes of about 2 mm width for each thickness.

The structure is characterized experimentally by spectroscopic reflectometry (Cary spectrometer) and spectroscopic ellipsometry (UVISEL from HORIBA Jobin Yvon). Models are crucial to spectroscopic ellipsometry data interpretation. Dispersion laws specific to our Al mirror (200 nm thick) are determined by measurements before silica deposition. To take into account its roughness and oxidation, the Al mirror is modeled by a bulk aluminum basis covered with an extra thin layer (3 nm) of effective medium defined in the Bruggeman approximation. With 41% of alumina and 59% of Al, the model fits the measured reflectivity (83% at 260–280 nm). Modeling is precious in understanding the different contributions to experimental contrast, notably through the knowledge of the exact reflectivity. Ellipsometric data after silica deposition are also consistent with the model.

2.3.2. Coating with inorganic absorber

For assessment of detection limits, small amounts of titanium dioxide are sputtered on the sample. Indeed, TiO_2 is strongly absorbent in the wavelength range of 260–280 nm (a 3-nm thick layer roughly yields a 25% absorption, measured with a Cary spectrometer). The sample is then covered with a layer of SPR 220 positive photoresist (Shipley) which is lithographically processed, to obtain spots of diameter 100 μm, with a 500 μm center-to-center distance (a typical pitch of biological spots on biochips). The sample is then ion-etched, before removing the photoresist with acetone. This provides a calibrated absorption, an essential data for further evaluation of biological results.

2.3.3. Biological coating of the sensor chip

A similar biochip is coated with the MetRS protein. The biochip is first covered with photoresist protecting the support, and lithographically processed to leave holes of the very same geometry as the TiO_2 spots (complementary geometry of the mask used for TiO_2), ready for chemical modification.

2.3.3.1. Production and purification of histidine-tagged methionyl-tRNA synthetase. An *Escherichia coli* histidine-tagged methionyl-tRNA synthetase (MetRS) was produced from a plasmid derived from pBSM547 (Mellot et al., 1989). The polyhistidine tag allows immunodetection of the MetRS with antiHis-Ab. By site-directed mutagenesis, the GCCTACTATG sequence encompassing the ATG start codon of methionyl-tRNA synthetase gene of pBSM547 was replaced by a GTCGAGTATGCACCATCACCATCACCAT sequence.

The obtained plasmid, named pBSM547-6His, was used to transform an *E. coli* strain JM101Tr (Hirel et al., 1988). Transformed cells were grown at 37 °C in 500 mL of a culture medium (1.6% bacto-tryptone, 1% bacto-yeast extract, 0.5% NaCl) containing 80 μg of ampicillin/mL and 0.3 mM isopropyl-1-thio-β-D-galactopyranoside. When the optical density of the culture reached 2.8 at 650 nm, cells were harvested and disrupted by sonication as described in Mellot et al. (1989). Cell extract, diluted in 15 mM of a 50 mM potassium phosphate buffer (pH 8) containing 300 mM NaCl, was applied on a Talon column (1 cm × 6 cm; Clontech Laboratories, inc.) equilibrated in the same buffer. Elution was carried out at a flow rate of 0.6 mL/min with a linear gradient of 0–250 mM imidazole in the same buffer (94 mM/h). The purified MetRS protein solution in 20 mM potassium phosphate buffer (pH 8) containing 0.1 mM EDTA was brought to 70% ammonium sulfate saturation and kept at 4 °C. Before use, enzyme aliquots were dialysed against 20 mM potassium phosphate buffer (pH 8.5).

2.3.3.2. Chemical modification of substrate. Chemical modification of surfaces was carried out by chemical vapour deposition of 3-aldehydopropyltrimethoxysilane (from United Chemical Technologies Inc.) at 50 °C, after activation by Ar/O_2 plasma treatment with a Diener Electronic plasma cleaner (20% O_2, 0.5 mbar, 100 W, 2 min). Slides were then heated at 100 °C under vacuum for 1 h. The protecting photoresist was removed with acetone, leaving aldehyde-functionalised spots, which will react readily with protein amino groups.

2.3.3.3. Immobilisation of MetRS and complexation with antiHis-Ab. The biochip surface (36 mm^2) was incubated at room temperature for 15 h by placing a coverslip over 1.5 μL of a buffered solution of 100 μM MetRS (20 mM potassium phosphate, 450 mM KCl, pH 8.5) containing 40 mM sodium cyanoborohydride (Sigma–Aldrich). A humidified atmosphere prevented evaporation of the liquid film between slide and coverslip, and sodium cyanoborohydride stabilized covalent binding by reducing Schiff bases.

Slides dedicated to UV detection of coated MetRS were washed at pH 8, with a solution containing 10 mM Tris–HCl, 150 mM NaCl and 0.2% Triton X-100 (buffer A). Remaining slides, dedicated to UV detection of complexation with a specific antibody (antiHis-Ab) were passivated at room temperature for 15 h by placing a coverslip over 1.5 μL of an ethanolamine solution (100 mM ethanolamine, 40 mM sodium cyanoborohydride, 20 mM potassium phosphate, pH 8.5), washed with buffer A, incubated with Penta-His Alexa Fluor 647 conjugate (Qiagen, 1/2000 in buffer A) for 2 h and washed again with buffer A. Prior to imaging, all slides were soaked in deionized water and dried. According to literature, $\varepsilon_{280\,nm}$ of Immunoglobulin G is 1.4×10^{-3} $cm^2/\mu g$ (Pierce Biotechnology, 2004). This value must be increased by 5% to take into account the presence of Alexa Fluor 647 in the above conjugate (result not shown).

3. Results and discussion

Optimization of the set-up and biochip multilayer structure is first performed with TiO_2. Then, experiments with proteins are carried out on biochips that showed the best surface absorption contrast. Thanks to contrast enhancement, we demonstrate that it is possible to image these protein spots.

3.1. Calibration: images with titanium dioxide spots

3.1.1. Images on variable dielectric thicknesses

Images assembled from line scans are made with the set-up presented in Section 2, providing the reflectivity map of the biochip.

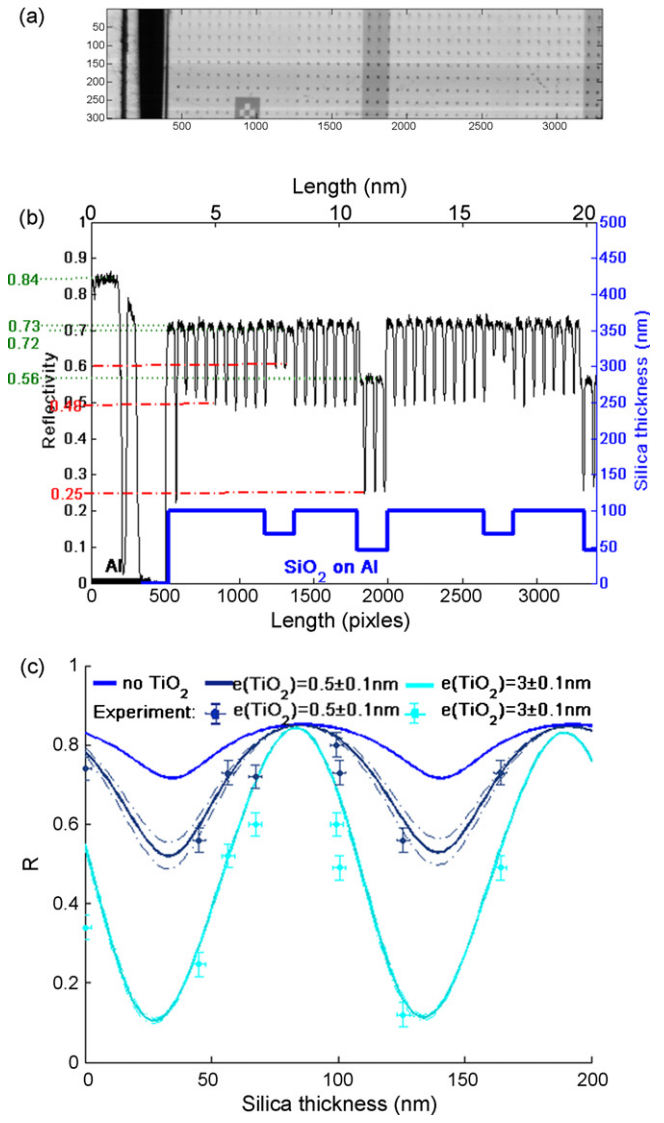

Fig. 3. (a) Image of a sample with TiO_2 spots on three different thicknesses of silica. On the left part of the image, a piece of raw deposited aluminum of reflectivity 83% is displayed. (b) Reflectivity profile along a line of TiO_2 spots: the absorption is enhanced for some silica thicknesses. (c) Experimental points (dots) obtained for eight thicknesses of the silica layer, inside the spots (3-nm thick TiO_2 layer) and outside the spots (0.5-nm thick TiO_2 layer). Results of the electromagnetic modeling (solid line) are superposed on the experimental points.

Fig. 3(a) displays the image obtained on a sample with three different thicknesses of silica on Al, covered with TiO_2 spots. In total, eight different silica thicknesses are obtained by combining several deposits and etching processes.

To determine the absolute reflectivity, measurements are normalized by using bare aluminum of known reflectivity (determined by spectroscopic reflectometry measurements). This piece of aluminum is at the left of the image displayed in Fig. 3(a). The profile along the long axis is given in Fig. 3(b). Fig. 3(c) shows the experimental reflectivity as a function of silica thickness e together with the simulations. The simulation curves are obtained including the extra 3 nm composite layer on Al described in Section 2.3. TiO_2 layer thickness is determined through transmission spectroscopic measurement and has a standard deviation of 0.1 nm. Due to instrumental characteristics and different deposit and etching process, silica thickness standard deviation is estimated to ±2.5 nm. The reflectivity oustide the lithographically defined spots reveals that

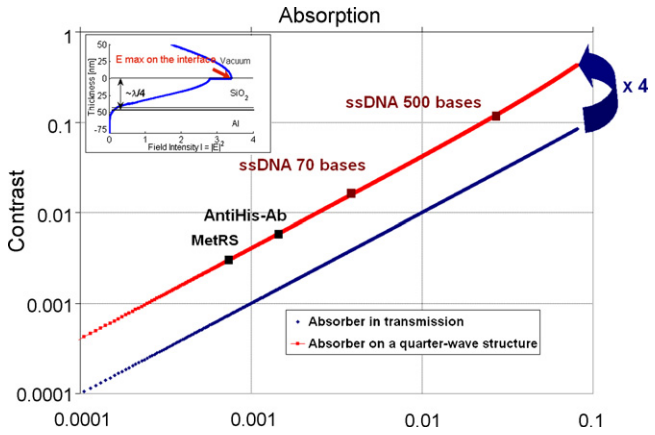

Fig. 4. Contrast in log scale of contrast absorption in transmission (blue diamonds) and absorption-induced reflectivity contrast on a quarter-wave spacer dielectric thickness (red squares). The quarter wave structure enables a contrast enhancement by a factor of 4. Calculated biological contrast of ssDNA, MetRS and antiHis-Ab (Table 1) are plotted for a density of 4×10^{12} molecules/cm^2. Inset shows the irradiance profile (square of the electric field) for quarter wave silica spacer at $\lambda = 280$ nm and $\theta = 45°$. The electric field is maximal at the interface (whereas it would be zero for half-wave spacer). (For interpretation of the references to color in this figure legend, the reader is referred to the web version of the article.)

3 nm-thick TiO_2 layer is not totally etched away: a 0.5-nm-thick layer still remains. The error in reflectivity is estimated to ±3%, due to fabrication fluctuations and optical adjustment. For small local variation ΔR the error is then $(1 \pm 0.03) \times \Delta$R, and will not appreciably influence the determination of protein absorption in Section 3.2.

As expected, the TiO_2-induced contrast markedly depends on the silica thickness e: the absorption is higher (reflection minima are deeper) when the absorbent is at an antinode of the electric field. The data are consistent altogether. Notably the TiO_2 data are validated as well, so that the reflection changes vs. absolute single-pass absorption can be calibrated.

3.1.2. *Sensitivity*

We compare here the contrast obtained as a function of silica thickness e, and more precisely for quarter-wave and half-wave thicknesses. In Fig. 4, we plot on a log scale the absorption-induced reflectivity contrast $\Delta R/R$. For a quarter-wave silica layer, the irradiance antinode is located just at the air–silica interface. The experimental reflectivity of the quarter-wave silica layer structure being $R = 0.72$, the contrast is enhanced by a factor of 4.0 ($\equiv (1+\sqrt{R})^2/\sqrt{R}$) for weak absorption (Seraphin and Bottka, 1965; Benisty et al., 1998). For biological elements displaying an absorption in the per mil order, such an enhancement is obviously interesting. This quarter-wave situation is therefore chosen to image proteins bound to the biochip surface.

3.1.3. *Resolution and dynamic*

By analyzing the set-up imaging properties, we found that it has a modest spatial frequency bandwidth: for example the relative decrease at sharp edges is 15% per pixel, 6–7 pixels being needed for full decrease. The pixel size is 26 μm, and the magnification is $\gamma = 3.8$. It corresponds to a low modulation transfer function (MTF) at pixel frequency $19.2 \times 3.8 = 73$ lines/mm in the object plane. The self-MTF of the linear array is estimated to 0.45 (Maezzo et al., 2006). Other losses in contrast are due to the microscope objective and tube lens, uncorrected from aberration. Nevertheless, the spatial resolution remains sufficient to image typical 100 μm spots.

3.2. Images of biochip coated with proteins

Images of biochips coated with 70 bases ssDNA have already been observed in our group (Reverchon et al., 2006). Imaging of proteins is much more challenging since their absorption is at least one order of magnitude weaker (Table 1). Fig. 5 gives images of the optimized biochip coated with MetRS before and after complexation with an anti-polyHis specific antibody.

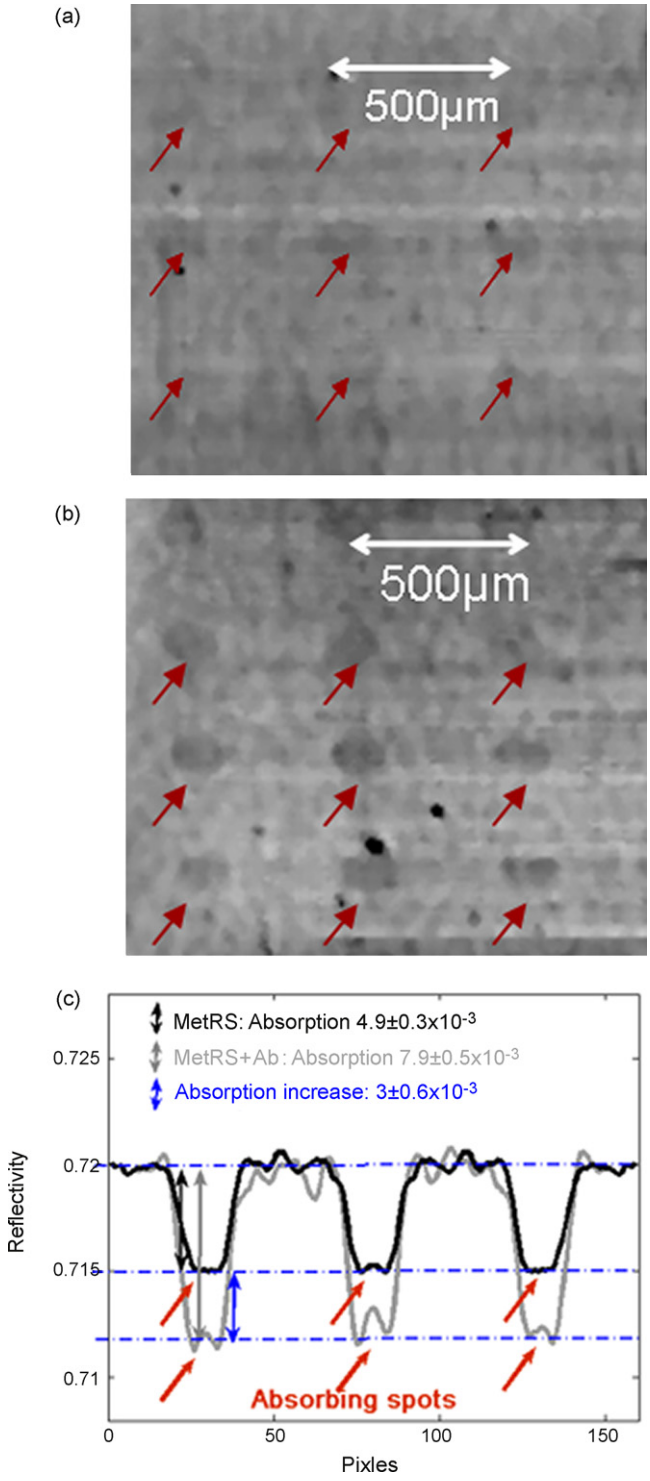

Fig. 5. Biochip images of (a) MetRS and (b) MetRS complexed with an antiHis-Ab. (c) Average line profiles on three spots. Spots are indicated by arrows.

The absorption profile is obtained by averaging the absorption on several spots. The mass extinction coefficient of MetRS is 1.72×10^{-3} cm^2/µg, corresponding to a monolayer absorption $A_{280\,nm} = 0.73 \times 10^{-3}$ without contrast enhancement (Table 1). At 280 nm, absorption due to silanisation of the surface, and to polyhistidine tag can be neglected. With a 4.0 contrast enhancement, the contrast is then $\Delta R/R = 4.0 \times A_{280\,nm}$. With $R = 0.72$ and a MetRS surface density of 4×10^{12} molecules/cm^2 (maximum density for monolayer coverage, Section 2.1.2), the calculated reflectivity decrease ΔR is 2.1×10^{-3}. The drop measured experimentally with the uncomplexed protein is $\sim 4.9 \pm 0.3 \times 10^{-3}$, averaged on a number of 45 spots profiles. The somewhat higher absorption can be explained by a larger than expected number of proteins at the chip surface and optical effects such as scattering due to roughness and optical index contrast. The density of proteins on the surface is not well calibrated. To have a better insight in the amount of proteins present on the chip surface, ellipsometric analysis was carried out on a chip homogeneously coated with MetRS (6 mm × 6 mm). With an optical index between 1.35 and 1.6 in visible (Vörös, 2004), a layer of thickness between 3.2 nm and 5.4 nm is obtained for the dried protein. In solution, the volume of the protein is ~5 nm × 5 nm × 10 nm. Therefore, it is reasonable to conclude that we are close from monolayer coverage.

The reflectivity drop measured on the biochip coated with MetRS complexed with an antiHis-Ab (Fig. 5(b)) is $7.9 \pm 0.5 \times 10^{-3}$, averaged on 45 spot profiles, to be compared to the experimental value of $4.9 \pm 0.3 \times 10^{-3}$ with the MetRS alone. If one assumes that the roughness of the surface and the optical index contrast are similar in the two cases, the measured $\Delta R = 3 \pm 0.6 \times 10^{-3}$ increase in absorption upon antibody complexation can be attributed to the antibody absorbance. The corresponding single-pass absorption $A_{280\,nm} = (\Delta R/R)/4$ is $1.04 \pm 0.02 \times 10^{-3}$, corresponding to a surface density of $2.8 \pm 0.5 \times 10^{12}$ Ab/cm^2 (Table 1). Such a value is close to that of a densely packed IgG monolayer (650 ng/cm^2 i.e. 2.6×10^{12} Ab/cm^2 (Esser, 1988)). Thus, the surface density of antibodies in the monolayer is maximal. This may explain why a 1:1 MetRS/Ab stochiometry cannot be reached. Furthermore, no absorption increase was observed after incubation of a MetRS-coated slide in the presence of anti-mouse IgG Horseradish-Peroxidase-linked whole antibody (Amersham Biosciences, 1/2000) (data not shown). This establishes the specificity of the interaction observed between antiHis-Ab and MetRS.

4. Conclusion and perspectives

A UV reflective set-up using an AlGaN spectrally selective detector, together with optimized multilayer structures, proved to be sensitive enough to detect monolayers of proteins/DNA, without need for labeling. These multilayer structures consist of an Al mirror covered with UV transparent dielectric (here silica). The experimental results on an inorganic test system (TiO_2 "spots") demonstrated a contrast amplification by a factor of 4.0, consistent with detailed multilayer analysis including roughness and oxidation layers. With this set-up capable of measuring sub 10^{-3} single-pass absorption, UV absorption of a protein layer was observed experimentally as well as absorption increase due to specific antibody complexation.

The measurement of uncomplexed protein absorption gave a value larger than expected for monolayer coverage. It can be explained by a larger amount of immobilized proteins. Optical effects such as scattering due to surface roughness are also likely. The absorption increase measured after specific antibody complexation, in good agreement with the expected value, validates biological recognition imaging.

The sensitivity of our set-up is readily sufficient to control the grafting of proteins, and the complexation with an antibody. Experiments were carried out with line-scan detectors, not well adapted to real-time acquisitions. Currently, new generation detectors, arrayed in 2D, are elaborated in Thales Research and Technology (Reverchon et al., 2007). They also display a signal-to-noise ratio compatible with monolayer biological imaging. With the same absorption detection set-up and optimized reflective biochip, these 2D imagers should enable multiplex real-time imaging. Future developments will include guiding structures that might offer extra photonic improvements and the design of a set-up compatible with UV detection of biological events in aqueous solutions.

Acknowledgements

The authors acknowledge Sylvain Blanquet, Arnaud Brignon, and Simone Cassette for fruitful discussions, and Jean-Michel Vignolle for image processing.

References

Bass, M., Stryland, E.W.V., Williams, D.R., Wolfe, W.L., 2000. Optical Society of America, Handbook of Optics, vol. I., 2nd ed. MacGraw-Hill, New York.

Benisty, H., Stanley, R., Maier, M., 1998. J. Opt. Soc. Am. A 15, 1192–1201.

Bruggeman, D.A.G., 1935. Ann. Phys. 24, 636–679.

Cassio, D., Waller, J.P., 1971. Eur. J. Biochem. 20 (2), 283–300.

Du, H., Fuh, R.A., Li, J., Corkan, A., Lindsey, J.S., 1998. Photochem. Photobiol. 68, 141–142.

Esser, P., 1988. Nunc Bull. 6.

Fasman, G.D., 1975. Handbook of Biochemistry and Molecular Biology, vol. I. CRC Press, Cleveland, OH.

Gill, S.C., von Hippel, P.H., 1989. Anal. Biochem. 182 (2), 319–326.

Hirel, P.H., Lévêque, F., Mellot, P., Dardel, F., Panvert, M., Mechulam, Y., Fayat, G., 1988. Biochimie 70, 773–782.

Maezzo, G., Reverchon, J.L., Duboz, J.Y., Dussaigne, A., 2006. IEEE Sensors J. 6 (4), 957–963.

Mechulam, Y., Schmitt, E., Maveyraud, L., Zelwer, C., Nureki, O., Yokoyama, S., Konno, M., Blanquet, S., 1999. J. Mol. Biol. 294, 1287–1297.

Mellot, P., Mechulam, Y., LeCorre, D., Blanquet, S., Fayat, G., 1989. J. Mol. Biol. 208, 429–443.

Murphy, B.D., 2001. Fundamentals of Light Microscopy and Electronic Imaging. Wiley-Liss, New York.

Pace, C.N., Vajdos, F., Fee, L., Grimsley, G., Gray, T., 1995. Protein Sci. 4 (11), 2411–2423.

Peterson, A.W., Heaton, R.J., Georgiadis, R.M., 2001. Nucleic Acids Res. 29 (24), 5163–5168.

Pierce Biotechnology, 2004. Technical ressource TR0006.0.

Reverchon, J.L., Meyer, C., Mazzeo, G., Cassette, S., 2006. Proc. SPIE no. 6398-25.

Reverchon, J.L., Robot, J.A., Truffer, J.P., Caumes, J.P., Mourad, I., Brault, J., Duboz, J.Y., 2007. Proc. SPIE no. 6744-9.

Seraphin, B.O., Bottka, N., 1965. Phys. Rev. 139 (2A), 560–564.

The general issue is how much a surface layer absorption translates into a reflectivity change. This is accessible through full multilayer simulations, but was also addressed in the early days of photo/electroreflectance measurements, e.g. by Seraphin on semiconductor, leading to two Seraphin coefficients relating the reflectivity modulation to the real and imaginary parts of the dielectric perturbation. This was revisited later for interference effects when probing multilayers. Essentially, the reflected amplitude has a basic term $\sqrt{R}$, and an in-phase term due to the upwards radiation of the absorbing layer, which turns out to be of the form $(\alpha l)(1+\sqrt{R})^2/2$ (see ref (Benisty et al., 1998) Eq. (17) with $r_2 = 0$, $t_2 = 1$). The squared modulus of the total reads $R + \sqrt{R}(\alpha l)(1+\sqrt{R})^2$ to first order in absorption. The relative change is thus as indicated. To our knowledge, only needlessly sophisticated versions of this basic physics exist in the literature.

Smith, D.Y., Shiles, E., Inokuti, M., 1985. In: Palik, E.D. (Ed.), Handbook of Optical Constants of Solids. Academic Press, San Diego, pp. 369–406.

Smith, E.A., Corn, R.M., 2003. Appl. Spectrosc. 57 (11), 320–332.

Stroud, D., 1998. Superlattice Microstruct. 23, 567–573.

Vörös, J., 2004. Biophys. J. 87, 551–553.

Windt, D.L., 1998. Comput. Phys. 12, 360–370.